

Processes and Their Limitations in Oxygen Depolarized Cathodes: A Dynamic Model-Based Analysis

Maximilian Röhe, Fabian Kubannek, and Ulrike Krewer*^[a]

Oxygen depolarized cathodes (ODCs) are key components of alkaline fuel cells and metal–air batteries or of chlor-alkaline electrolysis, but suffer from limited oxygen availability at the reaction zone. Dynamic analysis is a highly suitable approach to identify the underlying causes, especially the limiting steps and process interactions in such gas diffusion electrodes. Herein, a one-dimensional, dynamic, three-phase model for analyzing the oxygen reduction reaction in silver-based ODCs is presented. It allows for a detailed evaluation of the electrochemical reaction, the mass transport processes, and their interaction. The model also reveals that the depletion of reactant oxygen in the liquid electrolyte is caused by the current-dependent change of the gas–liquid equilibrium as the limiting subprocess. The phase equilibrium, in turn, depends on the slow mass transport of water and hydroxide ions in the liquid phase. Key parameters are the location or size of the gas–

liquid interface within the electrode. Profiles of local concentrations and partial pressures of different species reveal a steep gradient of oxygen in the liquid phase, but no limitation in oxygen mass transport in the gas phase. Dynamic simulations with potential steps allowed the identification of different time constants to separate overlapping processes. Accordingly, the mass transport of water and hydroxide ions was identified as the slowest process that strongly influenced the dynamic response of all species, including oxygen, and of the current. The characteristic time constant of the mass transport of water and hydroxide ions across the liquid phase within the ODC is determined to be $\tau_{\text{mt, H}_2\text{O}} \approx 0.176$ s, whereas the time constant of oxygen mass transport into the reaction zone is several magnitudes smaller: $\tau_{\text{mt, O}_2} \approx 1.70 \times 10^{-6}$ s. Finally, a sensitivity analysis confirms that the overall performance is best improved by adjusting mass transport properties in the liquid phase.

Introduction

Over 60% of all goods in the chemical industry contain chlorine as a basic chemical. In 2017, 89 million tons of chlorine were produced worldwide. By using traditional NaCl membrane electrolysis, this corresponds to a consumption of 195 800 GWh electrical energy per year and the emission of 82 million tons of CO₂.^[1] An energy-saving alternative is given by advanced chlor-alkali electrolysis with oxygen depolarized cathodes (ODCs), which reduces the required energy by about 30%.^[2] Here, in contrast to the standard process, no hydrogen is produced as a coproduct, but oxygen is consumed at the cathode.^[3] The centerpiece of this technique is the silver catalyst based gas diffusion cathode,^[4] at which the oxygen reduction reaction (ORR) takes place [Eq. (1)]:



The ODCs themselves consist of a porous structure of silver particles and a polytetrafluoroethylene (PTFE) coating of 300 to 1000 μm thick. Typical operating conditions are NaOH con-

centrations of around 10 M, a temperature range from 80 to 90 °C,^[2,5] and current densities of 4 to 6 kA m^{-2} .^[6] Under these conditions, silver shows the same electrochemical activity as that of a platinum catalyst.^[7] However, regardless of the great importance of the ORR, the key drivers for the observed high current densities of the ODCs and the underlying limiting processes are not well understood. Essential properties such as the local distribution of the gaseous and liquid phase within the electrode are unknown.^[8] Because the solubility of oxygen in the liquid electrolyte is poor due to the high ionic concentration and temperature, the attained high current densities are presently not explainable.^[9] The behavior of the ORR and the ODCs in alkaline media have been investigated in several studies: Blizanac et al. examined the reaction pathway of the ORR on silver single-crystal surfaces with rotating ring disk electrodes.^[10] The electrochemistry of oxygen in concentrated NaOH electrolyte was evaluated by Zhang et al.^[11] Later Pinnow et al. presented a model that describes the stationary performance of ODCs under various working conditions.^[12] The ODCs were characterized under industrial working conditions by Moussallem et al., with varying catalyst particle size distributions, PTFE and silver contents, and porosities.^[8] Clausmeyer et al. performed examinations with different NaOH concentrations in the electrolyte.^[13] In 2018, Botz et al. uncovered information about local activities directly at the electrode surface.^[9] However, the interplay of mass transport, processes at the gas–liquid interface, and reaction kinetics are not well under-

[a] M. Röhe, F. Kubannek, Prof. U. Krewer
Institute of Energy and Process Systems Engineering
Technische Universität Braunschweig
Franz-Liszt-Str. 35, 38106 Braunschweig (Germany)
E-mail: u.krewer@tu-braunschweig.de

stood, although this knowledge is essential for understanding the overall performance drivers and limiting factors. An appropriate, not yet applied, method to explore this issue is dynamic model-based analysis.

As shown previously in multiple studies, dynamic simulation provides information on the importance and interaction of mass transport, reaction mechanisms, and kinetics or geometrical structures; this is difficult to access in steady-state simulations. Examples of complex dynamic analysis and methods are the identification of reaction kinetics by using small sinusoidal signals,^[14] that is, electrochemical impedance spectroscopy; or state and concentration estimation from large sinusoidal signals,^[15] that is, nonlinear frequency response analysis. A notable, tangible alternative is given by the evaluation of potential steps (multistep chronoamperometry), chronoamperometry, or potentiometry. These methods have been successfully used, among other things, for the identification of transport and reaction processes in direct methanol fuel cells^[16] or to investigate the limiting factors for the ORR in metal–air batteries.^[17]

To explore the performance-limiting subprocesses of the ODC and to lay the foundation for a systematic improvement, herein, a dynamic, one-dimensional, three-phase model of the porous ODC for the ORR is introduced. To the best of our knowledge, it is the first dynamic model of an ODC and the first ODC model, in general, that takes the mass transport of water and hydroxide ions within the liquid phase and the corresponding phase equilibrium into consideration, so that the location of the gas–liquid interface can be identified. In contrast to stationary models, for example, the state-of-the-art thin-film flooded agglomerate model by Pinnow et al.,^[12] time constants can be simulated for a deeper analysis of the limiting factors and their interaction. Herein, polarization curves taken from the literature are used to validate the model. Next, dynamic simulations are evaluated to determine the relevant time constants and the limiting processes of the system. Finally, the evaluation is completed with a sensitivity study to show the impact of model parameters on the overall performance of the ODC. Through this procedure, we show that the mass transport of water and, particularly, hydroxide ions in the liquid electrolyte is determined as the overall restricting factor.

Model Concept and Assumptions

The ODC consists of a porous structure of silver particles and PTFE. Whereas silver serves as the heterogeneous catalyst for the ORR, PTFE is needed for the hydrophobic properties of the porous structure, to prevent a breakthrough of the aqueous NaOH electrolyte.^[2] Under operating conditions, the ODC is impinged by oxygen from one side and by the liquid electrolyte from the other side (cf. Figure 1). Due to the combination of the hydrophilic silver catalyst and hydrophobic PTFE, only a part of the ODC gets flooded, so that three different segments within the ODC are expected. The section facing the oxygen inlet contains a pure gas phase, whereas the section facing the

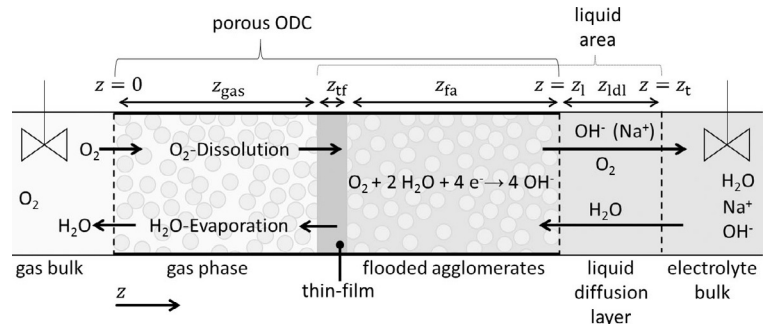


Figure 1. Schematic view of the model, including reactions and mass transport.

electrolyte is electrolyte flooded. Between the interface of both phases, the three-phase area is located. Processes occurring directly at the interface are the evaporation of water and the dissolution of oxygen into the electrolyte. Due to poor solubility of oxygen into the electrolyte, it is estimated that the ORR [Eq. (1)] takes place in the first few nanometers of the electrolyte.^[9,12] In addition to the transport of oxygen into the reaction zone, the provision of water and removal of hydroxide ions are mass transport processes.

To transfer the complex behavior of the ODCs to a suitable dynamic model, the following assumptions are made:

- 1 No pressure drop occurs within the electrode.
- 2 The temperature in the electrode is constant and homogeneous.
- 3 A complete ORR [Eq. (1)] is assumed. Possible incomplete ORR with hydrogen peroxide as a final product is not considered, due to the high catalytic activity of silver for reducing hydrogen peroxide.^[18]
- 4 Due to the high overpotential, the anodic current is negligible; hence the kinetics can be described with the Tafel equation.
- 5 The location of the gas–liquid interface is stationary over time.
- 6 Within the electrolyte, electroneutrality is assumed.
- 7 Because the reaction zone in the electrode is very thin and the catalyst and electrolyte are highly conductive, no internal voltage distribution is considered.
- 8 The high concentration of NaOH results in a low viscosity of electrolyte; thus, a liquid diffusion layer between the ODC and bulk electrolyte has to be considered, even if the bulk electrolyte itself is ideally stirred.
- 9 A gaseous diffusion layer is not relevant. As shown later, the diffusion length in the gas phase does not contribute significantly to the total mass transport resistance and would not affect the ODC performance.
- 10 In all liquid sections, multicomponent diffusion is described by Maxwell–Stefan diffusion. Because the concentrations of hydroxide ions and water are both about 10^6 times higher than that of the oxygen concentration, the influence of oxygen diffusion on water and hydroxide diffusion is negligible.

- 11 The change of the electrolyte concentration due to the ORR leads to a change of electrolyte density (see Figure 14 in the Appendix). With the further assumption of local stationary phases, an overlying convection is assumed, to consider the according change in electrolyte volume. To calculate this flux, the simplification $c_{\text{total}} = c_{\text{total}}(z = 0, t = 0)$ is used (see Figure 10 in the Appendix). The error is less than 0.8%; a more in-depth error estimation is given in the Appendix. Further convection caused by water evaporation and oxygen dissolution is implemented in both phases.
- 12 The concentration of Na^+ is calculated from the equation for electroneutrality. To consider its influence on mass transport, the binary diffusion coefficient, $D_{\text{H}_2\text{O,NaOH}}^{\text{liq}}$ of NaOH versus H_2O within the liquid electrolyte is calculated with the concentrated solution theory, which takes OH^- and Na^+ into account.^[19]
- 13 In the ODC, the gradients in the through-plane direction (z direction) are decisive. A homogeneous distribution of the phases and their components in the x and y directions in-plane is assumed.

The one-dimensional, three-phase, thin-film-model is divided into four spatially resolved sections. As shown in Figure 1, three of them are located within the porous ODC: a pure gas phase; a thin film; and a flooded porous structure, which is denoted as flooded agglomerates hereafter. The thin film represents the interface of liquid and gas phases within the electrode; this approach is a common method for modeling phase boundaries with a high specific interface.^[20] Typical values for the thin-film thicknesses are between 25 and 300 nm.^[21] The fourth section is a liquid boundary layer beyond the electrode. For the thin film, the flooded agglomerates and liquid diffusion layer, hereafter, the collective term liquid phase is used.

The gas phase contains exclusively gases, namely, oxygen and water vapor. Whereas oxygen is provided by the gas bulk phase on the left, water evaporates from the liquid phase at the right-hand side. Additionally, oxygen is dissolved in the thin film and transported into the flooded agglomerates, where the ORR occurs. The thin film itself is an exclusive transport layer, where no reaction takes place. The upstream liquid boundary layer is included because a significant diffusion resistance is expected.^[9]

Because a homogeneous distribution of the gas-liquid interface and concentrations in the x and y directions is assumed, the specific surface area of the interface ($S_{\text{interface}}$) is defined by Equation (2) and represents the phase interface area per geometric cross-sectional area of the electrode:

$$S_{\text{interface}} = \frac{A_{\text{phase interface}}}{A_{\text{geometric}}} \quad (2)$$

This parameter enables the one-dimensional model approach to meet the characteristics of a large gas-liquid interface within the ODC, as displayed in Figure 2. Because a steep

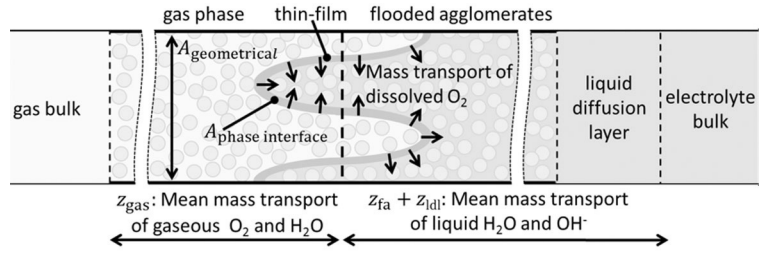


Figure 2. Mass transport processes at the gas-liquid interface.

oxygen gradient within a few nanometers of the gas-liquid interface is assumed,^[9] the meaningful area for dissolution and subsequent mass transport of oxygen is defined as the specific interface area (cf. Figure 2). The thin film represents the liquid side of the gas-liquid interface; hence the interface area is also relevant for the transport of water and hydroxide ions through the thin film. In contrast, the area for transport in the gas phase and for the transport of water and hydroxide ions in the flooded agglomerates is given by the geometric cross section.

Model Equations

Electrochemical reaction kinetics, double-layer capacitance, and internal resistance

The Faradaic current density, j_F , is modeled by using Faraday's law [Eq. (3)] and the Tafel equation [Eq. (4)]. All given current densities are referenced to the geometric cross section:

$$j_F = FAr \quad (3)$$

in which the reaction rate, r , is calculated from Equation (4):

$$r = k_0 a_{\text{O}_2} a_{\text{H}_2\text{O}}^2 \exp\left(\frac{(1-\alpha)F\eta_{\text{reaction}}}{RT}\right) \quad (4)$$

in which k_0 is the kinetic reaction rate constant, a_i are the activities of the species i , η_{reaction} is the overpotential, α is the anodic symmetry factor, and T is the temperature.

The concentration- and temperature-dependent activity, $a_{\text{H}_2\text{O}}$, is based on empirical studies of Balej,^[22] whereas for the oxygen activity, a_{O_2} , an approximately ideal behavior is assumed [Eq. (5)]:

$$a_{\text{O}_2} = f_{\text{O}_2} \frac{c_{\text{O}_2}}{c_{\text{O}_2}^\ominus} \quad (5)$$

Hence, a_{O_2} is calculated from the fugacity coefficient, $f_{\text{O}_2} = 1$; the standard concentration, $c_{\text{O}_2}^\ominus = 1 \text{ kmol m}^{-3}$; and the concentration of dissolved oxygen in the electrolyte, c_{O_2} .

The overpotential of the ORR, η_{reaction} , is defined as the difference between the open-circuit potential (OCP), E_{O_r} , and the potential in the reaction zone, E_{int} [Eq. (6)]:

$$\eta_{\text{reaction}} = E_{\text{int}} - E_0 \quad (6)$$

Ohmic potential losses can be calculated according to Ohm's law [Eq. (7)] as the difference between the external applied potential and the potential in the reaction zone:

$$E_{\text{ext}} - E_{\text{int}} = R_{\text{specific}} j \quad (7)$$

in which E_{int} is the potential in the reaction zone, which equals the external applied potential, E_{ext} under consideration of the specific Ohmic resistance, R_{specific} . The current density, j , is the sum of the Faradaic and capacitive current density: $j = j_F + j_{\text{dl}}$.

By assuming a constant double-layer capacitance, C_{dl} , the charge balance in the reaction zone is given by Equation (8):

$$C_{\text{dl}} \frac{dE_{\text{int}}}{dt} = j - F4r \quad (8)$$

Mass transport in the gas phase and processes at the gas-liquid interface

To model mass transport in the gas phase, the evaporation of water and dissolution of oxygen at the gas-liquid interface have to be taken into account as major effects. Because the absolute values of these two fluxes are typically unequal, in addition to diffusion, an overlaying convection has to be taken into account. This process is described by the bilateral non-equimolar diffusion, which is characterized by Fick's diffusion with an overlaying convective Stefan flow.^[23] The resulting species balance for $i = \{\text{H}_2\text{O}, \text{O}_2\}$ in the gas phase is given by Equation (9):

$$\frac{\partial p_i}{\partial t} \varepsilon = \frac{\partial^2 p_i}{\partial z^2} D_{ij}^{\text{gas,eff}} + \frac{\partial p_i}{\partial z} v_{\text{gas}} \quad (9)$$

in which p_i is the partial pressure of species i , t is the time, ε is the porosity, z is the location in the z direction, $D_{ij}^{\text{gas,eff}}$ is the effective binary diffusion coefficient, and v_{gas} is the velocity of the convective flow. $D_{ij}^{\text{gas,eff}}$ is calculated from the free diffusion coefficient, D_{ij}^{gas} ; porosity, ε ; and tortuosity, τ [Eq. (10)]:

$$D_{ij}^{\text{gas,eff}} = D_{ij}^{\text{gas}} \frac{\varepsilon}{\tau} \quad (10)$$

The tortuosity is approximated with the Bruggemann relationship: $\tau = \varepsilon^{-0.5}$.^[24]

To calculate the Stefan flow, a constant pressure of p_{total} is assumed. The only sinks and sources for both components are dissolution and evaporation at the gas-liquid interface, $z = z_{\text{gas}}$, and further inclusion of the ideal gas law results in the same convective velocity over the whole gas phase [Eq. (11)]:

$$\frac{dv_{\text{gas}}}{dz} = 0 \quad (11)$$

Thus, the velocity at every point in the gas phase exclusively depends on mass transfer over the gas-liquid interface [Eq. (12)]:

$$\dot{N}_{\text{total}}^{\text{convection}} = \dot{N}_{\text{H}_2\text{O}}^{\text{evaporation}} - \dot{N}_{\text{O}_2}^{\text{dissolution}} \quad (12)$$

The resulting convective mass flow, $\dot{N}_{\text{total}}^{\text{convection}}$, can also be described by the velocity of the flow in gaseous phase [Eq. (13)]:

$$\dot{N}_{\text{total}}^{\text{convection}} = \frac{p_{\text{total}}}{RT} v_{\text{gas}} \quad (13)$$

The evaporation of water is described by Raoult's law, in which the partial pressure of water, $p_{\text{H}_2\text{O}}^*$ directly at the gas side of the interface equals the vapor pressure, $p_{\text{H}_2\text{O}}^{\text{vap}}$ which is a function of the concentration of sodium hydroxide, c_{NaOH}^* and of water, $c_{\text{H}_2\text{O}}^*$ immediately at the interface. The vapor pressure dependence, $p_{\text{H}_2\text{O}}^{\text{vap}}(c_{\text{NaOH}}^*, c_{\text{H}_2\text{O}}^*, T)$, is taken from Hirschberg,^[25] c_{NaOH}^* and $c_{\text{H}_2\text{O}}^*$ are calculated by considering mass conservation during the evaporation process with the use of a steady-state mass balance [Eq. (14) and Figure 3]:

$$\dot{N}_{\text{H}_2\text{O}}^{\text{TF,out}} = \dot{N}_{\text{H}_2\text{O}}^{\text{evaporation}} = \dot{N}_{\text{H}_2\text{O}}^{\text{Gas,in}} \quad (14)$$

in which $\dot{N}_{\text{H}_2\text{O}}^{\text{evaporation}}$ is the mass flow of evaporating water, which equals the sink of water in the liquid phase, $\dot{N}_{\text{H}_2\text{O}}^{\text{TF,out}}$, as well as the source of water in the gas phase, $\dot{N}_{\text{H}_2\text{O}}^{\text{Gas,in}}$. By solving the given equations [Eqs. (9), (14), and (17)], a dynamic implementation of Raoult's law can be obtained. A detailed description of this procedure was reported by Schröder et al.^[17] For technical implementation, this approach is used to interpolate the concentrations and, in particular, the partial pressures from the center of an adjacent gas volume element and thin-film volume element at the gas-liquid interface to the common border between these volume elements (cf. Figure 3).

A similar method is implemented for the dissolution of oxygen into the electrolyte, for which the flux leaving the gas phase, $\dot{N}_{\text{O}_2}^{\text{Gas,out}}$, is equal to the flux entering the liquid electrolyte, $\dot{N}_{\text{O}_2}^{\text{TF,in}}$ [Eq. (15)]:

$$\dot{N}_{\text{O}_2}^{\text{Gas,out}} = \dot{N}_{\text{O}_2}^{\text{dissolution}} = \dot{N}_{\text{O}_2}^{\text{TF,in}} \quad (15)$$

Here, Henry's law comes into effect to determine the oxygen concentration, $c_{\text{O}_2}^*$ directly at the gas-liquid interface, depend-

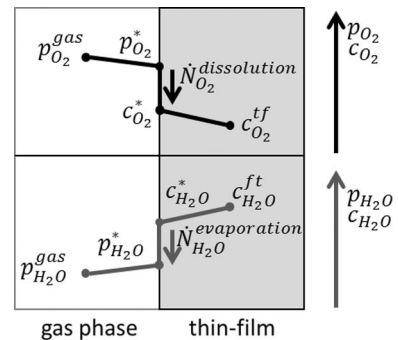


Figure 3. Illustration of a model of water evaporation and oxygen dissolution immediately at the gas-liquid interface. While oxygen is dissolved from the gas phase into the liquid electrolyte (top), water evaporates from the liquid electrolyte into the gas phase (bottom).

ing on the oxygen partial pressure, $p_{O_2}^*$. The inverse Henry constant for oxygen dissolution H_{O_2} is also a function of c_{NaOH}^* and $c_{H_2O}^*$ [Eq. (16)].^[26]

$$c_{O_2}^* = \frac{p_{O_2}^*}{H_{O_2}(c_{NaOH}^*, c_{H_2O}^*)} \quad (16)$$

The concentration-dependent functions of the water vapor pressure, $p_{H_2O}^{vap}(c_{NaOH}^*, c_{H_2O}^*)$ (Figure 12), and the Henry constant for oxygen dissolution, $H_{O_2}(c_{NaOH}, c_{H_2O})$ (Figure 11), are shown in the Appendix.

Mass transport in the thin film

Mass transport in the thin film is characterized by a diffusion process with an overlying convection of all species due to evaporation. This results from the assumption of a nonmoving interface and a constant thin-film volume. Because there are three species i in the thin film, $i = \{OH^-, H_2O, O_2\}$, for the diffusion process, the Maxwell–Stefan diffusion has to be taken into account [Eq. (17)]:

$$\frac{\partial c_i}{\partial t} = \sum_{j=1}^n \left(\frac{\partial^2 c_i}{\partial z^2} \frac{c_j}{c_{total}} - \frac{\partial^2 c_j}{\partial z^2} \frac{c_i}{c_{total}} \right) D_{ij}^{liq} + \frac{\partial c_i}{\partial z} v_{liq, evaporation} \quad (17)$$

Again, the oxygen concentration is very low; thus, no reasonable effect from oxygen diffusion to the diffusion of water and hydroxide ions is expected, which leads to $j = \{OH^-, H_2O\}$. As in the gas phase, the liquid evaporation velocity, $v_{liq, evaporation}$, is constant throughout the thin film [Eq. (18)]:

$$\frac{dv_{liq, evaporation}}{dz} = 0 \quad (18)$$

Thus, the velocity of the convective flow is directly proportional to the evaporation rate [Eq. (19)]:

$$v_{liq, evaporation} = \frac{\dot{N}_{H_2O}^{Gas, in}}{c_{H_2O}^*} \quad (19)$$

Mass transport in the flooded agglomerates

Mass transport within the flooded agglomerates is also described by Maxwell–Stefan diffusion with overlying convection, v_{liq} . The effective diffusion coefficient takes the porous structure into account and is calculated from Equation (10). Moreover, the sinks and sources due to the ORR have to be modeled; this yields the species balance in Equation (20)]:

$$\frac{\partial c_i}{\partial t} \varepsilon = \sum_{j=1}^n \left(\frac{\partial^2 c_i}{\partial z^2} \frac{c_j}{c_{total}} - \frac{\partial^2 c_j}{\partial z^2} \frac{c_i}{c_{total}} \right) D_{ij}^{liq, eff} + \frac{\partial c_i}{\partial z} v_{liq} - r \quad (20)$$

in which $i = \{OH^-, H_2O, O_2\}$ and $j = \{OH^-, H_2O\}$.

In addition to the above-described convection caused by evaporation, there is a further effect due to the reaction. The ORR causes a local change of water and hydroxide concentration, which consequently leads to a change in liquid density (cf. Figure 14 in the Appendix). Although the molecules of water and hydroxide per volume change depend on the reaction, the total concentration, c_{total} , stays almost totally constant (cf. Figure 10 in the Appendix). Consequently, the additional convection based on the density change between the reaction area and the electrolyte bulk phase can be described by the removal of additionally produced ions [Eqs. (21) and (22)]:

$$v_{liq, react}(z) = (|\nu_{H_2O}^{ORR}| - |\nu_{OH}^{ORR}|) \int_0^z \frac{r(z)}{c_{total}} dz \quad (21)$$

$$\frac{dv_{liq, react}}{dz} \neq 0 \quad (22)$$

in which r is the reaction rate, $\nu_{H_2O}^{ORR}$ is the stoichiometric factor of water, and ν_{OH}^{ORR} is the stoichiometric factor of hydroxide ions in the ORR.

Finally, the local total velocity, v_{liq} , for each location z can be calculated from the velocity of evaporation, $v_{liq, evaporation}$, and the location-dependent velocity of the reaction, $v_{liq, react}$ [Eq. (23)]:

$$v_{liq}(z) = v_{liq, evaporation} + v_{liq, react}(z) \quad (23)$$

Mass transport in the liquid diffusion layer

Mass transport in the liquid diffusion layer is described by the same equations as those of mass transport within the flooded agglomerates. In this layer, free diffusion occurs, so the free binary diffusion coefficient is used [Eq. (24)]:

$$\frac{\partial c_i}{\partial t} = \sum_{j=1}^n \left(\frac{\partial^2 c_i}{\partial z^2} \frac{c_j}{c_{total}} - \frac{\partial^2 c_j}{\partial z^2} \frac{c_i}{c_{total}} \right) D_{ij}^{liq} + \frac{\partial c_i}{\partial z} v_{ldl} \quad (24)$$

in which $i = \{OH^-, H_2O, O_2\}$ and $j = \{OH^-, H_2O\}$.

Because there are no sinks and sources in the liquid boundary layer, the convective velocity, v_{ldl} , is equal to that at $z = z_1$ (cf. Figure 1) of the flooded agglomerates [Eqs. (25) and (26)]:

$$v_{ldl} = v_{liq}(z = z_1) \quad (25)$$

$$\frac{dv_{ldl}}{dz} = 0 \quad (26)$$

Boundary conditions

Due to the high flux of oxygen in the gas bulk phase, the boundary conditions are defined by Equations (27) and (28):

$$p_{O_2}(z = 0) = p_{total} \quad (27)$$

$$p_{\text{H}_2\text{O}}(z = 0) = 0 \quad (28)$$

Because the electrolyte bulk phase is assumed to be ideally stirred, the concentration of oxygen is expected to be zero [Eq. (29)]:

$$c_{\text{O}_2}(z = z_t) = 0 \quad (29)$$

The amount of water in the electrolyte bulk phase can be calculated as a function of sodium hydroxide concentration,^[27] which is constant [Eqs. (30) and (31)]:

$$c_{\text{NaOH}}(z = z_t) = c_{\text{NaOH}}(z = z_t, t = 0) \quad (30)$$

$$c_{\text{H}_2\text{O}}(z = z_t) = f[c_{\text{NaOH}}(z = z_t, t = 0)] \quad (31)$$

Parameterization

The model was implemented in MATLAB. For parameter identification, data reported by Pinnow et al. was used.^[12] The examined ODC was manufactured through a spray method and contained 97 wt% silver and 3 wt% PTFE. The experiments were performed at 80 °C and with a NaOH molality of $m_{\text{NaOH}} = 11.25 \text{ mol kg}^{-1}$,^[12] which, under the given conditions, corresponded to a NaOH concentration of $c_{\text{NaOH}}(z = z_t) = 1.01 \times 10^4 \text{ mol m}^{-3}$.^[25,27] All further constant model parameters, set to their respective values obtained from experiments, are given in Table 1, and concentration-dependent parameters are listed in Table 2. The literature data were measured from $j = 0$ to 4 kA m^{-2} . Because the ORR will switch to the hydrogen evolu-

Table 2. Electrolyte concentration dependent variables; dependencies are shown in Figures 11 and 12 in the Appendix.

Name	Symbol	Unit	Source
inverse Henry constant ^[a]	H_{O_2}	$\text{Pa m}^3 \text{ mol}^{-1}$	[26]
activity of H_2O ^[b]	a_{O_2}		[35]
density of electrolyte	ρ	kg m^{-3}	[27]
water vapor pressure	$p_{\text{H}_2\text{O}}^{\text{vap}}$	Pa	[25]

[a] Extrapolated from $c_{\text{NaOH}} \leq 6 \text{ M}$, but as shown in Ref. [11] extrapolated values fit very well to experimental results for $c_{\text{NaOH}} \leq 12 \text{ M}$. [b] Extrapolated data from 343.15 to 353.15 K.

tion reaction at current densities close to the predicted limiting current, it is impossible to measure accurate ORR currents in this range. Therefore, hydrogen evolution free higher current densities have been simulated by the same authors.^[12,28]

Identified model parameters are the kinetic reaction rate constant, k_0 ; the specific interface area, $S_{\text{interface}}$; the specific resistance, R_{specific} ; and the length of flooded agglomerates, z_{fa} . The manually adjusted parameters that best reproduce the polarization curve documented by Pinnow et al.^[12] are given in Table 3. The corresponding curve in Figure 4 shows that the data matches very well; thus, the model can reproduce the steady-state polarization curve.

The identified specific gas-liquid interface area, $S_{\text{interfacel}}$ is about 2.5 times higher than the interface modeled by Pinnow et al.^[12] This deviation may originate from the strict consideration of the ion concentration dependent equilibrium at the gas-liquid interface applied herein. The ion concentration dependency of the phase equilibrium also enables an estimation

Table 1. List of constant parameters and operation conditions.

Parameter	Symbol	Unit	Value	Source
<i>Electrode geometry</i>				
electrode thickness	$Z_{\text{electrode}}$	m	300×10^{-6}	[12]
thin film thickness	Z_{tf}	m	60×10^{-9}	[12]
liquid diffusion layer thickness	Z_{dl}	m	50×10^{-6}	own estimation
porosity	ϵ		0.4	[12]
tortuosity	T		1.58	[24]
<i>Operation conditions</i>				
pressure in gas chamber ^[a]	p_{O_2}	Pa	1×10^5	[12]
NaOH concentration in electrolyte bulk ^[a]	$c_{\text{NaOH}}(z = z_t)$	mol m^{-3}	1.01×10^4	[12]
H_2O concentration in electrolyte bulk	$c_{\text{H}_2\text{O}}(z = z_t)$	mol m^{-3}	4.97×10^4	[25]
temperature ^[a]	T	K	353.15	[12]
<i>Electrochemical and kinetic data</i>				
OCP	E^0	V	0.216	[30]
symmetry factor ^[b]	α		0.15	[31]
no. electrons in the reaction	n_t		4	[10]
no. electrons in rate determining step	n_{rd}		1	[10]
double layer capacitance	C_{dl}	F m^{-2}	50	[32]
<i>Diffusion coefficients</i>				
binary gas diffusion coefficient	$D_{\text{O}_2, \text{H}_2\text{O}}^{\text{gas}}$	$\text{m}^2 \text{ s}^{-1}$	2.98×10^{-5}	[33]
binary liquid diffusion coefficient ^[b,c]	$D_{\text{O}_2, \text{H}_2\text{O}}^{\text{liq}}$	$\text{m}^2 \text{ s}^{-1}$	2.12×10^{-9}	[33, 34]
binary liquid diffusion coefficient ^[b,c]	$D_{\text{O}_2, \text{NaOH}}^{\text{liq}}$	$\text{m}^2 \text{ s}^{-1}$	3.16×10^{-9}	[33, 34]
binary liquid diffusion coefficient ^[d]	$D_{\text{H}_2\text{O}, \text{NaOH}}^{\text{liq}}$	$\text{m}^2 \text{ s}^{-1}$	1.19×10^{-9}	[19]

[a] Experimental operation conditions taken from Ref. [12]. [b] Measured with 6.5 M KOH. [c] Calculated by using a modified Wilke and Chang equation^[33], with $\Theta = 3.9$ and $a = 0.5$, for the best fit to the experimental data reported in Ref. [34]. [d] No NaOH data available; modeled for KOH with the NaOH viscosity reported in Ref. [27].

Table 3. Identified parameters that best reproduce the polarization curve.

Name	Symbol	Unit	Value
reaction kinetic rate constant	k_0	$\text{mol s}^{-1} \text{m}^{-2}$	165
specific interface	$S_{\text{interface}}$	$\text{m}^2 \text{m}^{-2}$	134
overall specific resistance	R_{specific}	Rm^2	1.9×10^{-5}
length of flooded agglomerates	Z_{fa}	m	11.5×10^{-6}
length of gas phase ^[a]	Z_{gas}	m	288×10^{-6}

[a] Calculated by $Z_{\text{gas}} + Z_{\text{tf}} + Z_{\text{fa}} = Z_{\text{electrode}}$

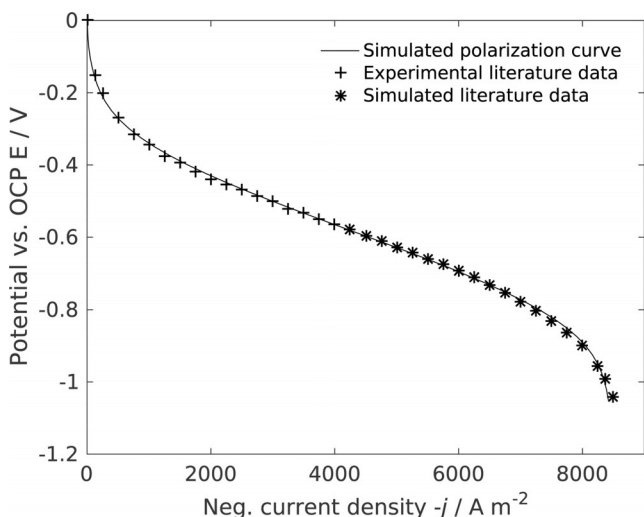


Figure 4. Simulated polarization curve in comparison with experimental data reported in the literature.^[12]

of the location of the gas–liquid interface. The average value of the distributed gas–liquid interface is located $11.5 \mu\text{m}$ from the end of the electrode facing the liquid side, so that only a small part of the ODC is flooded with the liquid electrolyte (Figure 2). Because the diameter of the pores of comparable ODCs is typically less than $1 \mu\text{m}$ ^[29] and PTFE has a strongly hydrophobic character, this value seems to be valid. Present theories about the shape of the gas–liquid interface are, for example, cylindrical electrolyte flooded agglomerates surrounded by the gas phase^[12] or microscopic gas channels reaching into the flooded electrode part.^[13] If assuming a regular cylindrical shape of the catalyst agglomerates in the electrode, which are oriented perpendicular to the electrode surface,^[28] agglomerate diameters of $d_{\text{ag}} = 0.62 \mu\text{m}$ are obtained. This comparably small diameter may indicate microscopic gas channels into the flooded agglomerates, an uneven surface following the catalyst particles, or a moving interface. As discussed in the section on parameter sensitivities below, all identified parameters have a characteristic influence on the polarization curve, which is indicated by different sensitivities of the overpotential to the parameters at kinetic, ohmic, and mass transport governed operation conditions. Nevertheless, the identified parameter set may not be unique. Reliable parameterization would require additional, especially dynamic, measurements that enable a

strict separation of slow and fast processes. However, based on the comparison to literature values, we assess the parameter set to be reasonable.

Results and Discussion

Steady-state analysis

To develop a deeper understanding of the processes within the ODC, the states underlying the simulated polarization curve (cf. Figure 4) are analyzed in the following section in detail. The electrode potential is referred to the open-cell potential, E^0 , of the simulated process conditions: $E = E_{\text{ext}} - E^0$. As shown in Figure 5a, the oxygen concentration is depleted strongly within the electrode close to the gas–liquid interface. The drop gets steeper with increasing negative current densities. Even at medium current densities of about 5 kA m^{-2} , dissolved oxygen can be found only in the first 200 nm of the flooded electrode section. Although only a small fraction of the catalyst is involved in the reaction, the kinetic losses are comparably low, which indicates a high catalytic activity of silver for the ORR in alkaline media. At higher current densities, only the region directly behind the interface stays electro-

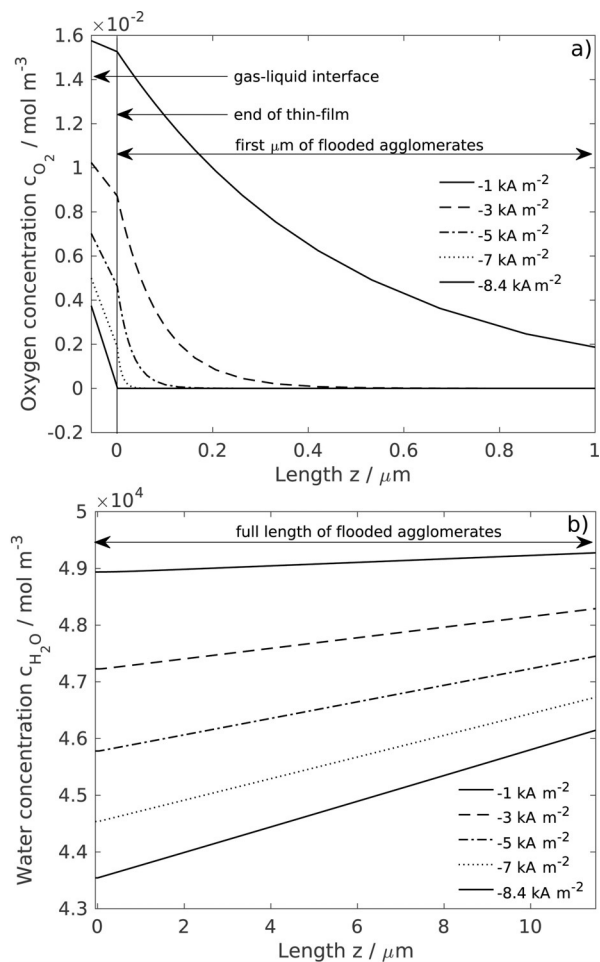


Figure 5. Dependence of simulated a) oxygen and b) water concentration profiles within the liquid phase on current density.

chemically active, which supports findings previously reported.^[9,12] Here, two major effects are identified, leading to the transport limitation of oxygen. First, for increasing current, more oxygen is consumed by the ORR, as indicated by the steeper gradient of oxygen concentration in the thin film and flooded agglomerates. Second, the higher reaction rate at higher currents causes an enrichment of the concentration of OH⁻ ions as the reaction product of the ORR and an accompanying decline in water concentration as an educt of the ORR (cf. Figure 5b). Because the Henry constant is a function of ion concentration (cf. Figure 11), the solubility of oxygen decreases at higher current densities and limits the amount of dissolved oxygen in the liquid electrolyte. This effect can be recognized by the decreasing oxygen concentration at the gas–liquid interface. The high sensitivity of oxygen solubility to the ion concentration also explains the mass transport impact documented in previous studies, even at low current densities of about 0.1 kA m⁻².^[28] The water concentration only decreases by 14.3% to 4.35 × 10⁴ mol m⁻³ at $j=8.4$ kA m⁻², whereas the ion concentration increases by 37.3% to 1.61 × 10⁴ mol m⁻³. Hence, no significant consequences result from the lower water concentration available for the reaction but do result in the previously mentioned change of the phase equilibrium. The change of water concentration at the interface of the flooded agglomerates to the liquid diffusion layer shows that not only is mass transport within the ODC important, but so is mass transport across the liquid diffusion layer.

To analyze the driving forces of the mass flow in the liquid phase, the fraction of mass flow driven by diffusion, $\dot{N}_i^{\text{diffusion}}$, in relation to the total mass flow, $\dot{N}_i = \dot{N}_i^{\text{diffusion}} + \dot{N}_i^{\text{convection}}$, of species i is calculated by $x_i = |\dot{N}_i^{\text{diffusion}}|/|\dot{N}_i|$. For all species, the mass flow in the liquid phase is dominated by diffusion. As shown in Figure 6, the oxygen mass transport, in particular, is almost entirely diffusion driven, due to the steep concentration gradient and low concentration in the flooded agglomerated. Because oxygen is depleted with increasing depth into the flooded agglomerates, an evaluation of oxygen mass transfer is only possible directly behind the thin film (cf. Figure 6). For

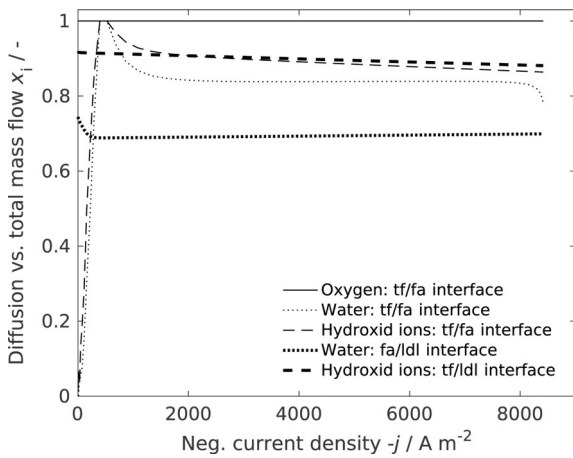


Figure 6. Fraction of mass flow driven by diffusion in comparison with the total mass flow in the flooded agglomerates as a function of the current density at various locations; tf=thin film, fa=flooded agglomerates.

water and hydroxide ions, lower values are obtained: $x_{\text{H}_2\text{O}} \approx 70\%$ and $x_{\text{OH}^-} \approx 90\%$, respectively. Because the concentration gradient of water or hydroxide ions is practically the same, but opposite in direction within the flooded agglomerates, the diffusion mass flow is in the same range for both species. In contrast, the convection-based mass flow of each species is proportional to the concentrations, which is higher for water than that for the hydroxide ions. Accordingly, relative to the total mass transfer, the diffusion-driven mass transfer is lowest for water and highest for oxygen. The high ratio of convective mass flow of water and hydroxide at low currents close to the thin film is caused by the evaporation of water.

The concentration-dependent equilibrium at the gas–liquid interface also affects the partial pressures and mass transfer in the gas phase. The vapor pressure of water decreases by a factor of 2.93 (cf. Figure 12) and the inverse Henry constant increases by a factor of 5.81 (cf. Figure 3) upon increasing the current to a maximum. As a consequence of changes to the equilibrium for water evaporation and oxygen dissolution, the velocity of convection decreases from $v_{\text{gas}}(j=0)=7.18 \times 10^{-5}$ ms⁻¹ to $v_{\text{gas}}(j=j_{\text{max}})=1.78 \times 10^{-5}$ ms⁻¹. As a result, the partial pressure of water decreases with higher current densities. To gain a deeper impression of the outlined findings and to separate the different effects, as well as to obtain information about their interaction, dynamic results are presented in the next section.

Dynamic analysis

In this section, dynamic simulations with potential steps are presented; these enable the separation and identification of the interactions in the reaction and different mass transfer processes. To cover typical operation current densities of 4 to 6 kA m⁻²,^[6] potential steps from $E=0.55$ to 0.65 V and from $E=0.6$ to 0.55 V versus OCP have been chosen; these correspond to steady-state currents of 3.76 and 5.30 kA m⁻². The variations in applied potential, E , and current density, j , with respect to the system response are depicted in Figure 7. Two significantly different time constants can be distinguished: a rapid and strong change of the current within milliseconds and a slow relaxation of smaller amplitude within 5 s. The response signal to steps up and down in potential are identical, but with opposite sign. The rapid change observed for the positive and negative steps results from the charging or discharging of the double layer. The second observed, significantly larger, time constant results from mass transfer within the ODC following the consumption and production of species, as well as from the potential-sensitive charge transfer. In Figure 8a, it can be seen that, after the potential step, both water and oxygen concentrations require approximately 5 s to reach the new steady state; no overshooting is observed. Because the diffusion pathways of water and hydroxide ions between the reaction zone and bulk phase are much longer than the diffusion pathway of oxygen through the thin film into the reaction area, at least two time constants for the mass transfer are expected. Indeed, in Figure 8a, one may see that the oxygen concentration change is significantly

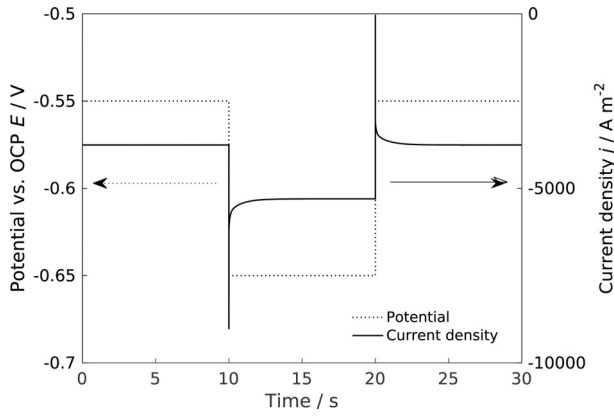


Figure 7. Electrode potential and current dependence on time for a potential step of -0.55 to -0.65 V versus OCP at $t=10$ s and back at $t=20$ s.

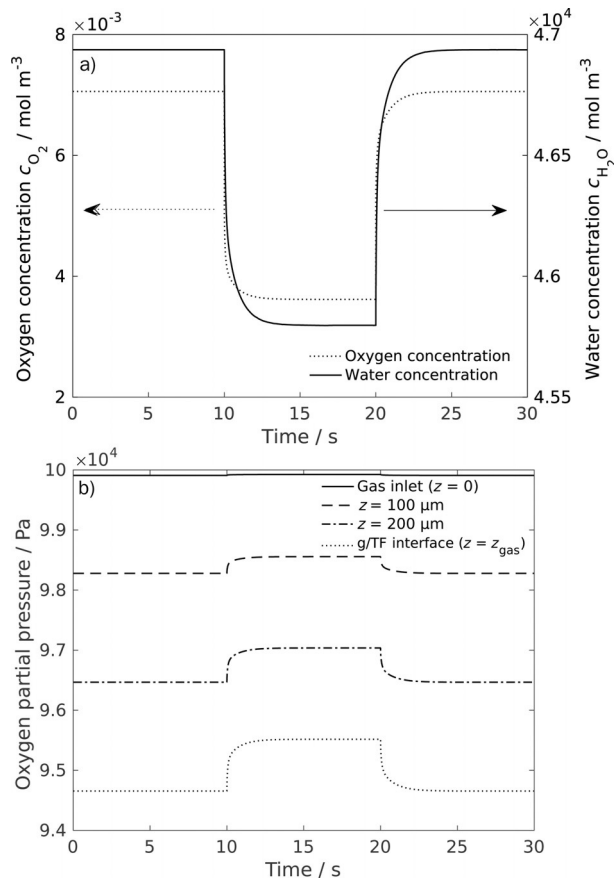


Figure 8. a) Concentration responses of oxygen and water at the thin film liquid interface for a potential step of -0.55 to -0.65 V versus OCP at $t=10$ s and back at $t=20$ s, and b) the response of oxygen partial pressure at various locations.

steeper in the first second, but then slows down and reaches steady state at the same time as that of water. Comparing both plots in Figure 8, the concentration of water and oxygen at the boundary between the thin film and flooded agglomerates shows the same relaxation time as that of the current. This supports the conclusion that the shift of the phase equi-

librium couples both processes and dominates the dynamic response.

To analyze the time behavior of oxygen mass transport, the oxygen partial pressure in the gas phase has to be taken into account (see Figure 8b). Unexpectedly, the oxygen partial pressure rises simultaneously with stronger current. Two aspects can be identified. First, although more oxygen is consumed at higher current densities, the partial pressure of oxygen in the gaseous phase is increasing. Second, a comparison of the dynamics in the gas phase with the dynamics in the liquid phase shows almost the same shape and time constants, thus suggesting similar rate-determining steps. The rise in partial pressure can be attributed to a lowering of the water activity due to the production of hydroxide ions and the consumption of water, which decrease the oxygen solubility and vapor pressure of the electrolyte. For a deeper analysis, the time constants of the different mass transport processes can be approximated by Equation (32), under the valid assumption that the mass transfer is dominated by diffusion (see Figure 6):

$$\tau_{mt} \approx \frac{\Delta z^2}{D} \quad (32)$$

Because the oxygen partial pressure in the gaseous phase is increasing with higher current densities, the decreasing concentration of oxygen in the liquid phase at high current densities can be attributed to mass transport through the liquid phase, but not the gas phase. Inserting the thickness of the thin film as the diffusion length, a time constant of about $\tau_{mt,O_2} \approx 1.70 \times 10^{-6}$ s is calculated, which explains the significantly steeper fall of oxygen concentration than that of water in the first milliseconds after the potential step. For the mass transport of water and hydroxide ions between the reaction zone and the bulk phase, the overlapping time constants for effective diffusion in the porous structure of the flooded agglomerates, τ_{mt,H_2O}^{fa} and free diffusion in the liquid diffusion layer, τ_{mt,H_2O}^{ldl} have to be determined separately. Here, $\tau_{mt,H_2O}^{ldl} \approx 2.10$ s and by considering the porous structure [cf. Eq. (20)], a value of $\tau_{mt,H_2O}^{fa} \approx 0.176$ s is calculated. Due to the more rapid decrease in water concentration within about 1 s after the potential jump, on one hand, and the comparably long relaxation time to a new steady state of about 5 s, on the other hand (cf. Figure 8a), it can be concluded that the observed current density response is dominated by both mass transport in the flooded agglomerates and mass transfer in the liquid diffusion layer.

By combining the given information, it can be concluded that the process governing the dynamic behavior is slow mass transport of water and hydroxide ions through the liquid phase. Thus, their interplay with the phase equilibrium dominates the overall performance of the ODC.

Parameter sensitivities

To analyze the influence of the parameters for the evaluated electrode on the model output systematically, a local sensitivity analysis has been performed. The relative sensitivity, s_v , of the electrode potential, E_{Ext} to the parameter ς is determined from

Equation (33):

$$s_{\zeta} = \frac{\frac{E_{\text{ext}}}{\zeta} - \frac{E_{\text{ext}}^{\circ}}{\zeta^{\circ}}}{\frac{E_{\text{ext}}}{\zeta} - \frac{E_{\text{ext}}^{\circ}}{\zeta^{\circ}}} \quad (33)$$

in which ζ° denotes the value at the reference point and ζ is one for an increased or decreased parameter. Every parameter is varied by $\pm 5\%$: $\zeta = \zeta^{\circ} \cdot (1 \pm 0.05)$. The results given in Figure 9 are the mean of individual results of the positive and negative modified parameter. A high sensitivity of a parameter indicates a strong impact on the electrode potential, whereas a sensitivity close to zero indicates a negligible influence.^[36]

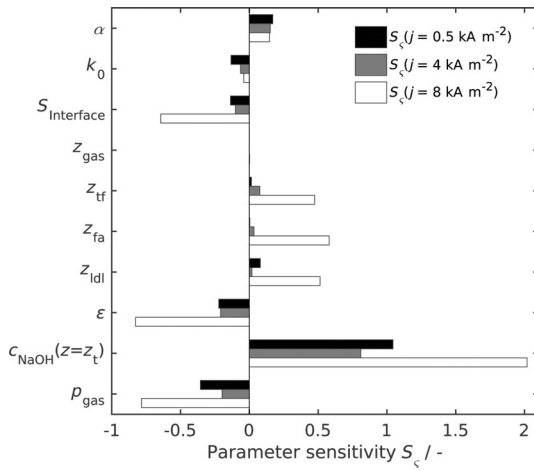


Figure 9. Relative sensitivity, s_{ζ} , of the electrode potential to parameter variation of $\pm 5\%$ for three different constant current densities. Upon increasing c_{NaOH} , the current density of $j = 8 \text{ kA m}^{-2}$ could not be reached; thus only results for negative variation are shown.

Sensitivity analysis is presented for three characteristic regimes (cf. Figure 4): current densities of 4 kA m^{-2} as the industrial operating point, 0.5 kA m^{-2} as a kinetically governed operating point, and 8 kA m^{-2} as a mass transport governed operating point. For the evaluation, it is important to note that the slope of the polarization curve (cf. Figure 4) at 0.5 and 8 kA m^{-2} is much higher than that at 4 kA m^{-2} . Consequently, the parameters may exhibit smaller sensitivities at 4 kA m^{-2} than those at the other two points of the polarization curve. The varied parameters are further segmented into three different groups: kinetic parameters, structural and geometric parameters, and operation conditions (Figure 9).

As expected, the reaction rate constant, k_0 , affects the potential most at low currents. Although the performance at high current densities is dominated by mass transport, the performance shows significant sensitivity to high catalyst activity and a high catalyst surface. The symmetry factor, α , has a medium-high influence on the ODCs over the entire operation range.

To evaluate the sensitivity of the thickness of different electrode sections individually, the boundary condition $z_{\text{gas}} + z_{\text{tf}} +$

$z_{\text{fa}} = z_{\text{electrode}}$ was ignored. The thickness of the liquid phase, z_{lf} , has the largest influence on the cell potential; the length of the gas phase, z_{gr} , is not selective. This supports the prior conclusion of a limitation resulting from the mass transport of water and hydroxide ions across the liquid phase, whereas mass transport in the gas phase is not limiting. The ODC performance may thus be improved through a reduction of the flooded part, especially at higher currents. This could be achieved with a more hydrophobic ODC, by using either smaller pores or a higher amount of hydrophobic PTFE. Because a lower porosity and tortuosity, due to smaller pores, and a lower reaction rate, due to a smaller catalyst surface, would lead to a decrease in cell performance, optimum levels of these parameters have to be found. Furthermore, the length of the flooded part, z_{far} , cannot be arbitrarily reduced because a certain space is required for a large specific interface. The same holds for the diffusion layer in the liquid electrolyte: a thicker liquid diffusion layer has, especially at higher current densities, a negative impact on the operation conditions of the electrode. Herein, an approach to improve the electrode performance is given by an artificial convective flow to reduce the diffusion layer thickness, z_{idl} . Moreover, the thin film acts as an additional diffusion resistance for oxygen dissolved by the gaseous phase,^[20] thus the high sensitivity of the thin-film thickness at diffusion-limiting current densities is explainable. It has been shown that the thin-film thickness, in particular, dominates the shape of the polarization curve.^[21] Finally, the specific interfacial area, $S_{\text{interface}}$ between liquid and gas phases is particularly important at high current densities, at which oxygen solubility limits the performance.

The great sensitivity to electrolyte concentration, $c_{\text{NaOH}}(z = z_l)$, emphasizes the previously discussed solubility limitation by the ion concentration at the gas-liquid interface. Previous studies have shown that the highest current densities for the ORR could be achieved with electrolyte concentrations of 5 M .^[13] We suggest that process conditions with high concentrations of over 5 M lead to mass transport limitations. However, because the hydroxide ions are the desired product of the ORR in advanced chlor-alkali electrolysis, the only way for a higher efficiency of the process is a faster removal of ions. The potential is sensitive to oxygen partial pressure. The decrease in the electrode potential with increasing pressure, p_{gas} , results from lower mass transfer limitations of oxygen due to the higher amount of dissolved oxygen in the electrolyte. Although better performance with higher pressure is documented,^[13] it has to be mentioned that the pressure of oxygen can only be increased over a defined range to avoid a breakthrough of gas to the electrolyte side.^[8] Also notable is the sensitivity for pressure, even at low current densities, which is in agreement with the results of previous studies, that mass transport influences ODC losses,^[28] even at kinetically controlled current densities.

Conclusions

The first dynamic three-phase model of a porous ODC for advanced chlor-alkali electrolysis has been presented. Suitable

model parameters were partly obtained from the literature and partly identified from published polarization curves. It was shown that, under industrial operation conditions, the ORR only took place close to the gas-liquid interface because of the depletion of dissolved oxygen. The consumption of water and the production of hydroxide ions leads to a significant change of the phase equilibrium with current density, which causes a lower solubility of oxygen in the liquid electrolyte. This effect intensifies at higher reaction rates and causes a total depletion of oxygen, and thus, the limiting current. Water is sufficiently available for the reaction and does not limit the maximum current density in a direct way. A deeper dynamic evaluation of this behavior revealed that the removal of ions from the reaction area was the slowest process. It has a significant impact not only on stationary performance, but also on the full dynamic behavior of all concentration profiles, and thus, of the dynamic response. In this context, it was also shown that only a few micrometers of the ODC were flooded with the liquid electrolyte under industrial working conditions. Hence, dynamic analysis is a highly potent method to reveal the interaction of processes in the ODC and to determine its state. Dynamic measurements should be conducted for reliable, unique parameterization and for further validation of the model.

A sensitivity analysis of the kinetic, geometric, and process parameters indicated that an improvement of the ODC performance could be affected most with better mass transport properties in the liquid phase, for example, through a smaller level of flooding within the electrode or a smaller liquid diffusion layer.

Appendix

Error estimation

For all concentration-dependent calculations, the assumption of a constant total concentration, $c_{\text{total}} = c_{\text{total}}(z=0, t=0)$, is used. As shown in Figure 10, the respective error is less than 0.8% [Eq. (34)]:

$$\left| \frac{c_{\text{total}}(c_{\text{NaOH}}) - c_{\text{total}}(c_{\text{NaOH}}(z, z_1, t, 0))}{c_{\text{total}}(c_{\text{NaOH}}(z, z_1, t, 0))} \right| \leq 0.008, \quad (34)$$

for $c_{\text{NaOH}} \in [1.05 \times 10^4, 1.75 \times 10^4 \text{ mol m}^{-3}]$

Concentration-dependent parameters

As observed in Figure 11, the inverse Henry constant is highly sensitive to water, and thus, the hydroxide concentration increases over the simulation range by a factor of 5.81.^[26]

Depending on the water and hydroxide concentration, the vapor pressure of water decreases over the simulation range by a factor of 2.91 (see Figure 12).^[25]

As shown in Figure 13, based on the enrichment of hydroxide ions, the water activity decreases by a factor of 2.22.^[35]

The concentration change of the liquid electrolyte leads to a volume change, and thus, to a convective flow (see Figure 14).^[27]

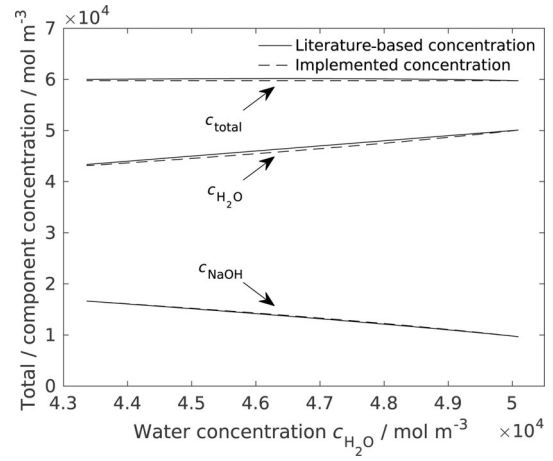


Figure 10. Total, water, and sodium hydroxide concentration of liquid electrolyte, calculated based on Hirschberg 1999^[25] and implemented in the model, depended on the modeled water concentration in the range of the simulation at $T=353.15$ K.

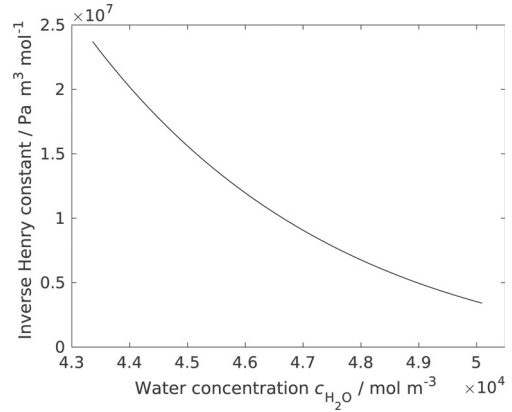


Figure 11. Inverse Henry constant over water concentration at $T=353.15$ K, hydroxide concentration according to Figure 10.

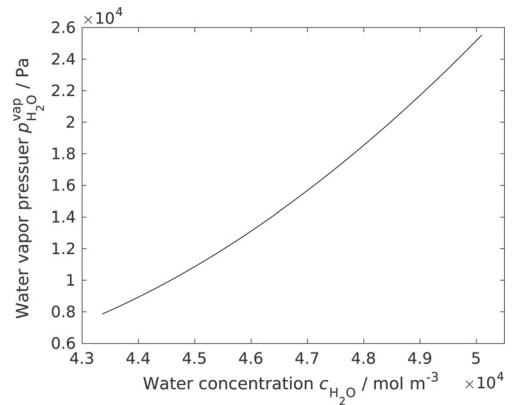


Figure 12. Vapor pressure of water as a function of water concentration at $T=353.15$ K, hydroxide concentration according to Figure 10.

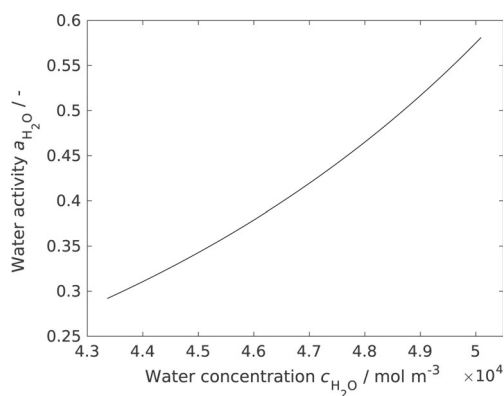


Figure 13. Activity of water as a function of water concentration at $T=353.15$ K, hydroxide concentration according to Figure 10.

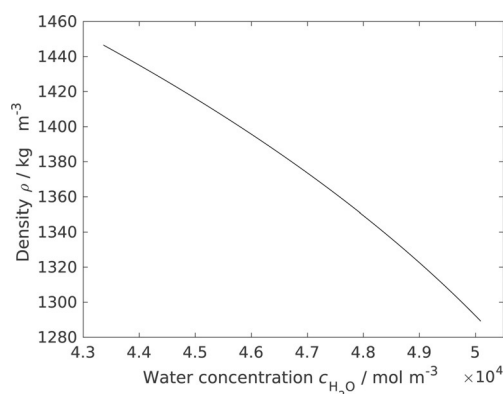


Figure 14. Density of electrolyte as a function of water concentration at $T=353.15$ K, hydroxide concentration according to Figure 10.

Acknowledgements

We are thankful to the Deutsche Forschungsgemeinschaft for funding this research in the framework of the Forschergruppe (FOR 2397) Multi-scale analysis of complex three-phase systems: oxygen reduction on gas-diffusion electrodes in aqueous electrolyte.

Conflict of interest

The authors declare no conflict of interest.

Keywords: chlor-alkali electrolysis • computational chemistry • dynamic modeling • electrochemistry • interfaces

- [1] J. Kintrup, M. Millaruelo, V. Trieu, A. Bulan, E. S. Mojica, *Electrochem. Soc. Interface* **2017**, 26, 73–76.

- [2] I. Moussallem, J. Jrisen, U. Kunz, S. Pinnow, T. Turek, *J. Appl. Electrochem.* **2008**, 38, 1177–1194.
- [3] N. Chavan, S. Pinnow, G. D. Polcyn, T. Turek, *J. Appl. Electrochem.* **2015**, 45, 899–912.
- [4] T. F. O'Brien, T. V. Bommaraju, F. Hine, *Handbook of Chlor Alkali Technology*, Springer, Boston, **2005**.
- [5] L. Lipp, S. Gottesfeld, J. Chlistunoff, *J. Appl. Electrochem.* **2005**, 35, 1015–1024.
- [6] R. Kuwertz, I. G. Martinez, T. Vidakovic Koch, K. Sundmacher, T. Turek, U. Kunz, *Electrochem. Commun.* **2013**, 34, 320–322.
- [7] M. Chatenet, L. Genies Bultel, M. Aurousseau, R. Durand, F. Andolfatto, *J. Appl. Electrochem.* **2002**, 32, 1131–1140.
- [8] I. Moussallem, S. Pinnow, N. Wagner, T. Turek, *Chem. Eng. Process.* **2012**, 52, 125–131.
- [9] A. Botz, J. Clausmeyer, D. Ohl, T. Tarnev, D. Franzen, T. Turek, W. Schuhmann, *Angew. Chem. Int. Ed.* **2018**, 57, 12285–12289; *Angew. Chem.* **2018**, 130, 12465–12469.
- [10] B. B. Blizanac, P. N. Ross, N. M. Markovic, *J. Phys. Chem. B* **2006**, 110, 4735–4741.
- [11] C. Zhang, F. Ren, F. Fan, A. J. Bard, *J. Am. Chem. Soc.* **2009**, 131, 177–181.
- [12] S. Pinnow, N. Chavan, T. Turek, *J. Appl. Electrochem.* **2011**, 41, 1053–1064.
- [13] J. Clausmeyer, A. Botz, D. Ohl, W. Schuhmann, *Faraday Discuss.* **2016**, 193, 241–250.
- [14] U. Krewer, H. K. Yoon, H. T. Kim, *J. Power Sources* **2008**, 175, 760–772.
- [15] Q. Mao, U. Krewer, *Electrochim. Acta* **2012**, 68, 60–68.
- [16] U. Krewer, A. Kamat, K. Sundmacher, *J. Electroanal. Chem.* **2007**, 609, 105–119.
- [17] D. Schröder, V. Laue, U. Krewer, *Comput. Chem. Eng.* **2016**, 84, 217–225.
- [18] E. L. Littauer, *J. Electrochem. Soc.* **1979**, 126, 1924.
- [19] J. Newman, D. Bennion, C. W. Tobias, *Ber. Bunsenges. Phys. Chem.* **1965**, 69, 608–612.
- [20] C. Y. Yuh, J. R. Selman, *J. Electrochem. Soc.* **1984**, 131, 2062–2069.
- [21] F. G. Will, D. J. Bendaniel, *J. Electrochem. Soc.* **1969**, 116, 933–937.
- [22] J. Balej, *Collect. Czech. Chem. Commun.* **1996**, 61, 1549–1562.
- [23] B. Kögl, F. Moser, *Grundlagen der Verfahrenstechnik*, Springer, Vienna, **1981**.
- [24] J. van Brakel, P. M. Heertjes, *Int. J. Heat Mass Transfer* **1974**, 17, 1093–1103.
- [25] H. G. Hirschberg, *Handbuch Verfahrenstechnik und Anlagenbau*, Springer, Berlin, **1999**.
- [26] D. Tromans, *Ind. Eng. Chem. Res.* **2000**, 39, 805–812.
- [27] J. Olsson, I. A. Jernqvist, G. I. Aly, *Int. J. Thermophys.* **1997**, 18, 779–793.
- [28] S. Pinnow, Dr. Ing. Dissertation, Technische Universität Clausthal, **2013**.
- [29] M. Neumann, M. Osenberg, A. Hilger, D. Franzen, T. Turek, I. Manke, V. Schmidt, *Comput. Mater. Sci.* **2019**, 156, 325–331.
- [30] S. G. Bratsch, *J. Phys. Chem. Ref. Data* **1989**, 18, 1–21.
- [31] P. K. Adanuvor, *J. Electrochem. Soc.* **1988**, 135, 2509.
- [32] G. D. Polcyn, Ph.D. thesis, Technischen Universität Dortmund, **2018**.
- [33] B. E. Poling, J. M. Prausnitz, J. P. O'Connell, *The Properties of Gases and Liquids*, 5th ed., McGraw Hill, New York, **2000**.
- [34] M. Chatenet, M. Aurousseau, R. Durand, *Ind. Eng. Chem. Res.* **2000**, 39, 3083–3089.
- [35] G. Åkerlöf, G. Kegeles, *J. Am. Chem. Soc.* **1940**, 62, 620–640.
- [36] T. Danner, B. Horstmann, D. Wittmaier, N. Wagner, W. G. Bessler, *J. Power Sources* **2014**, 264, 320–332.